# Study of the Impact of Structural Parameters on the Dynamic Response of an Electronic Fuel Injector

Nao Hu[1, 2, *], Jianguo Yang[1, 3], Peilin Zhou[2], Ying Hu[1]

1. School of Energy and Power Engineering, Wuhan University of Technology, 430063, Wuhan, PRC;

2. Department of Naval Architecture, Ocean and Marine Engineering, University of Strathclyde, G4 0LZ, Glasgow, UK;

3. Key Laboratory of Marine Power Engineering &Technology, Ministry of Communications, 430063, Wuhan, PRC;

*. Corresponding author

## Abstract

The study concentrates on the effects of structural parameters of an electronic fuel injector on its dynamic response (the opening delay and the closing delay). The injector was developed for a marine medium-speed diesel engine. The dynamic response from the start of the control signal to the end of the needle valve closing were investigated. Firstly, a complete and detailed model of the electronic fuel injector was built and integrated into an optimisation model, where a MOGA was applied. Secondly, the importance and effects of main structural parameters on dynamic response were examined, as were their interactions. Finally, a Pareto optimum was obtained through scattering charts and comparisons were made between the baseline design and the optimal design. Results show that the control piston diameter, fuel oil inlet passage

* Email: nao.hu.0128@gmail.com (N. Hu)

diameter, fuel oil outlet passage diameter and their interactions are influential factors to the opening delay, while the fuel oil inlet passage diameter has the dominant effect on the closing delay. A small control piston diameter together with a small fuel oil inlet passage diameter contribute to a short opening delay, however, they lead to a significant increase in the closing delay. Moreover, a small closing delay prefers a large fuel oil inlet passage diameter. The selected Pareto optimum achieved a significant reduction in both the opening delay and the closing delay under three different rail pressures.

*Keywords*: electronic fuel injector; structural parameter; dynamic response; interaction; optimization

**Nomenclature**

| | | | |
|---|---|---|---|
| 1D | one dimensional | PID | proportional-integral-derivative |
| 2D | two dimensional | RSM | response surface method |
| ARMOGA | adaptive range multi-objective genetic algorithm | SPF | spring preload force |
| CPD | control piston diameter | SS-ANOVA | smoothing spline analysis of variance algorithm |
| Compact RIO | a real-time embedded industrial controller made by National Instruments | μGA | micro-genetic algorithm |
| DOE | design of experiments | | |
| ECU | electronic control unit | Functions and variables | |
| GA | genetic algorithm | $M$ | objectives number |
| HIL | hardware in loop | $f$ | function |
| HPCR | high pressure common rail | $j$ | variable |
| IPD | fuel oil inlet passage diameter | $K$ | a specific objective |
| I/O | input/output | $\vec{x}^*$ | Pareto design |
| LABCAR | a flexible test system developed by ETAS company | $\vec{x}_j$ | arbitrary design |

| | | | |
|---|---|---|---|
| MOGA | multi-objective genetic algorithm | | |
| NSGA-II | non-dominated sorting genetic algorithm II | Units | |
| NZD | nozzle orifice diameter | mm | millimetre |
| NZN | nozzle orifice number | MPa | mega Pascal |
| OPD | fuel oil outlet passage diameter | ms | millisecond |
| PLC | programmable logic controller | N | Newton |

# 1 Introduction

Nowadays, the HPCR system has gained significant attention and application as one of the most promising technologies for the control of internal combustion engines. The electronic fuel injector, one of the key components of HPCR systems, is of particular interest to researchers. Many studies have already been carried out around the injector nozzle area, and on the influences of nozzle types and nozzle numbers on the internal flow and cavitation performance, for example, Molina et al. [1] investigated the inner nozzle flow and cavitation development of elliptical orifices, in that study, four nozzles with different major axis orientation and eccentricity value were compared with each other and also with the standard nozzle. Benajes et al. [2], Payri et al. [3], and Han et al. [4] focused on nozzle orifice types for electronic fuel injectors, comparisons were made between a cylindrical nozzle and a conical one. He et al. [5], Moon et al. [6] and Salvador et al. [7] studied the effects of different nozzle hole arrangements and needle lift movements on the initial flow and cavitation development inside diesel injectors. However, to date, little attention has been paid to the influence of the nozzle parameters on dynamic response, i.e. the opening delay and closing delay.

Few studies were found in the literature which considers the impact of electronic fuel injector structural parameters on the dynamic response. Salvador et al. [8] compared the influences of a standard diesel fuel and biodiesels on the dynamic behaviour of a solenoid-operated injector. A change of the fuel oil outlet passage diameter from 0.246 mm to 0.27 mm was proposed to eliminate the needle lift and injection rate deviations between the two fuels. The deviations were caused by a higher viscosity of the biodiesel fuel comparing to the regular diesel fuel. Results showed that the opening delay of the biodiesel fuel was reduced significantly under low injection pressure to match that of the standard diesel fuel. Additionally, some related studies are also worth mentioning. Wang et al. [9] investigated the influence of control valve parameters on the flow and cavitation inside the control valve. Stefano Beccari et al. [10] predicted the mass injected by a gaseous fuel solenoid injector for spark ignition engines, with special attentions paid to a gas injector and to the complex needle motion during the opening and closing phases. Cheng et al. [11] investigated the impact of drive strategies on the power losses and dynamic response of a solenoid injector. As it can be seen that these studies focused on the dynamic response of the needle motion itself rather than on the opening delay and closing delay, and also left structural parameters such as the control piston diameter, fuel oil inlet passage diameter, fuel oil outlet passage diameter and the spring preload force at the needle valve out of their scope. Salvador et al. [12] investigated the impact of fuel temperature on injection dynamics, especially during the opening stage and closing stage. The delays were considered, but the structural parameters were still not included.

In this paper, the impact of the structural parameters of an electronic fuel injector on injector dynamic response of the opening delay and closing delay are carefully investigated, and the opening delay and closing delay are the two objectives to be minimised. Firstly, a complete and detailed 1D electronic fuel injector model was built in AMESim and was validated by using injection quantity data and average steady-state mass flow rate obtained from a HIL test rig. Then, an optimisation model was built in the modeFRONTIER software, where the 1D fuel injector model was included and a MOGA was applied for optimisation. Besides the impacts of the structural parameters, the interactions of them were also studied. Scattering charts were used for selecting Pareto designs and the sensitivity of the important parameters and interactions on the delays were examined using RSM.

One-dimensional (1D) models have frequently been built and adopted in many studies to predict the performance of electronic fuel injectors. R. Payri et al. [13] used a 1D model of a solenoid-driven common rail ballistic injector to study the influences of the inlet fuel temperature on injection rate. Seykens et al. [14] built a 1D model of an injector to analyse the elasticity of the injector needle valve and nonlinearities caused by the impact of the needle valve when it returns to its seat. Rahim et al. [15] implemented a 1D model to study the effect of temperature on diesel engine performance. The detailed modelling of a solenoid fuel injector and a third generation piezo injector were demonstrated by Payri et al. [16] and Salvador et al. [17] respectively.

Since two objectives are involved in this study, it is naturally a multi-objective problem. GA is born for solving multi-objective problems. It is based on the idea of the natural selection which obeys the law of "survival of the fittest". It can continually improves the average fitness level of a population by means of inheritance, mutation, selection and cross-over, eventually leading to an optimal design [18, 19, 20]. MOGA is the modified version of the classic GA which can find a set of multiple non-dominant solutions in a single run [21]. NSGA-II, one of the genetic algorithms, proposed by Deb et al. [22], was proven to have better performance of finding a diverse set of solutions and converging near the true Pareto front. Thus, in this paper, the NSGA-II algorithm is applied. The NSGA-II algorithm employs an elite-preserving strategy and an explicit diversity-preserving mechanism. According to the objectives, elitism is given to the corresponding designs. Designs with a higher elitism have priority to be selected. If two designs have the same elitism, the one with less crowding distance (proximity to other Pareto solutions) is assigned with a higher priority.

Pareto optimums are often adopted in multi-objective optimisation occasions, as shown in Fig. 1. Cases A-D can be considered as Pareto optimal cases due to the fact that none of them is out-performed by other cases. These cases can be grouped together to form a Pareto frontier [23]. The Pareto optimality can be defined as follows: for all designs and the corresponding $M$ objectives $f_k(\vec{x})$, where, $K$= 1, 2, …, $N$. The Pareto design $\vec{x}$ is defined as follows: for an arbitrary design j, there exists at least one objective, $k$,

meets the condition $f_k(\vec{x}_j) \preceq f_k(\vec{x}_i)$. MOGA's mission is to find the Pareto frontier whilst maintaining diversity in the results.

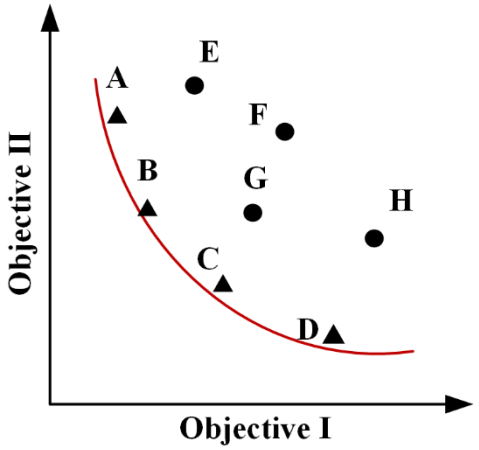


Fig. 1 Definition of Pareto optimums

RSM is a technique for performing optimisation based on a approximation model, which was built on a statistical technique of analysing the data generated by DOE [24]. Here, a non-parametric classification and regression method, the k-nearest method, was used to generate the response surface of influential parameters on the dynamic response. The k-nearest method [25] is an interpolation method with non-intensive computational requirements. Therefore, it is suitable for dealing with large data sets.

## 2 Specifications of the baseline injector

The baseline injector was designed and produced for the application on marine medium-speed diesel engines by an enterprise in China. The specifications of the baseline electronic fuel injector given by the manufacturer are reported in Table 1. The control piston diameter, fuel oil inlet passage diameter, fuel oil outlet passage diameter, nozzle orifice number, nozzle orifice diameter and spring preload force are represented

by the CPD, IPD, OPD, NZN, NZD and SPF respectively.

Table 1 Specifications of the baseline electronic fuel injector

| Specifications | Value |
|---|---|
| Control piston diameter (mm) | 6.5 |
| Fuel oil inlet passage diameter (mm) | 0.35 |
| Fuel oil outlet passage diameter (mm) | 0.45 |
| Nozzle orifice number | 9 |
| Nozzle orifice diameter (mm) | 0.27 |
| Spring preload force (N) | 149 |

# 3 Modelling of the electronic fuel injector

The 1D simulation model of the fuel injector was built in the AMESim software. The whole model was divided into three parts, i.e., the solenoid assembly, the injector body and the nozzle assembly. The detailed modelling process is demonstrated below.

## 3.1 Modelling of the solenoid assembly

In Fig. 2, C1 is the solenoid spring, C2 is the solenoid coil, C3 is the control valve, V1 is the low-pressure chamber and C4 is the ball valve. The left part of Fig. 2 shows a physical sketch of the solenoid assembly. The right part of the figure is part of a model built according to the physical sketch. The control valve C3 is the moving element of the solenoid assembly, which is raised up when the solenoid coil C2 is energised to take

the ball valve C4 off its seat, thus, opened the fuel oil outlet passage.

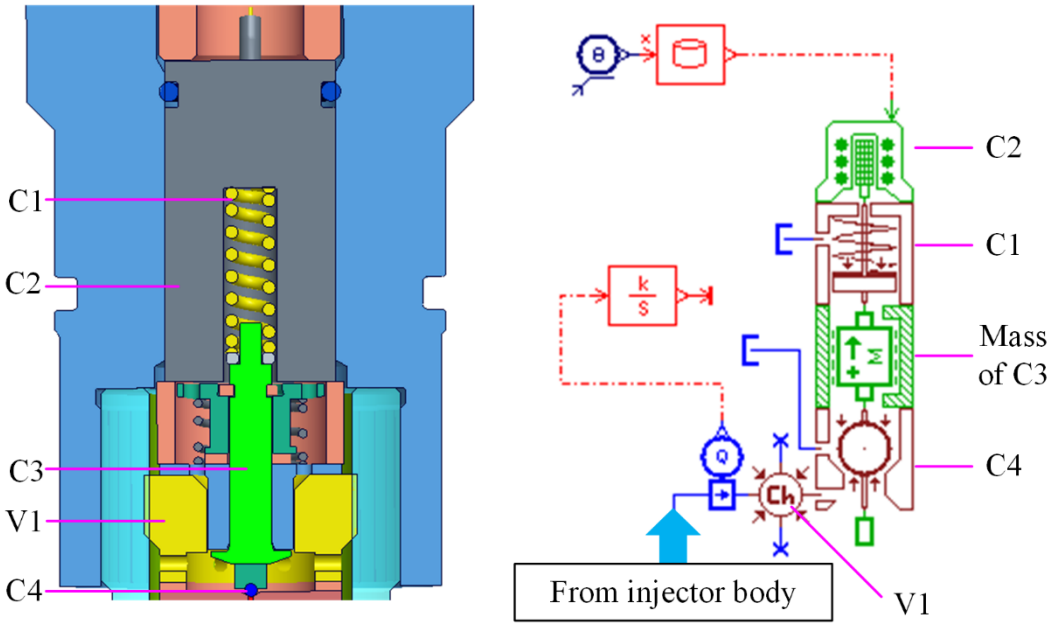


Fig. 2 Modelling of the solenoid assembly

Table 2 Parameters for the solenoid assembly

| Element | Diameter (mm) | Spring rate (N/m) | Volume ($cm^3$) | Mass (g) |
|---|---|---|---|---|
| C1 | - | 70 | - | - |
| C3 | - | - | - | 4 |
| V1 | - | - | 0.001 | - |
| C4 | 1.2 | - | - | - |

## 3.2 Modelling of the injector body

In Fig. 3, C5 is the control piston and C6 is the mandrel pushing rod. O1 and O2 stand for the control chamber fuel oil inlet passage and the fuel oil outlet passage respectively. L1-L5 represent oil lines. V0 is the rail volume and V2 is the control chamber volume.

A model of the injector body is shown on the right part of Fig. 3. In the model, a constant

pressure in the V0 was adopted to simulate the pressure in the common rail. The common rail is connected to the injector through high-pressure pipes, i.e. L2 and L4. The L2 leads to the control chamber via a short tube L3 and the control chamber fuel oil inlet passage O1. The L4 leads to the nozzle part. The volume V2 represents the volume of the control chamber. It is connected to the solenoid valve via the fuel oil outlet passage O2. The piston model C5 from the AMESim software includes a rod with the piston. In practice, no rod is seen in the control chamber, therefore, the diameter of the rod is set to zero in the model. Moreover, the mass, leakage, piston surfaces and stiffness of the C5 are also included according to their physical characteristics. Lines L5 represent the fuel oil return lines.

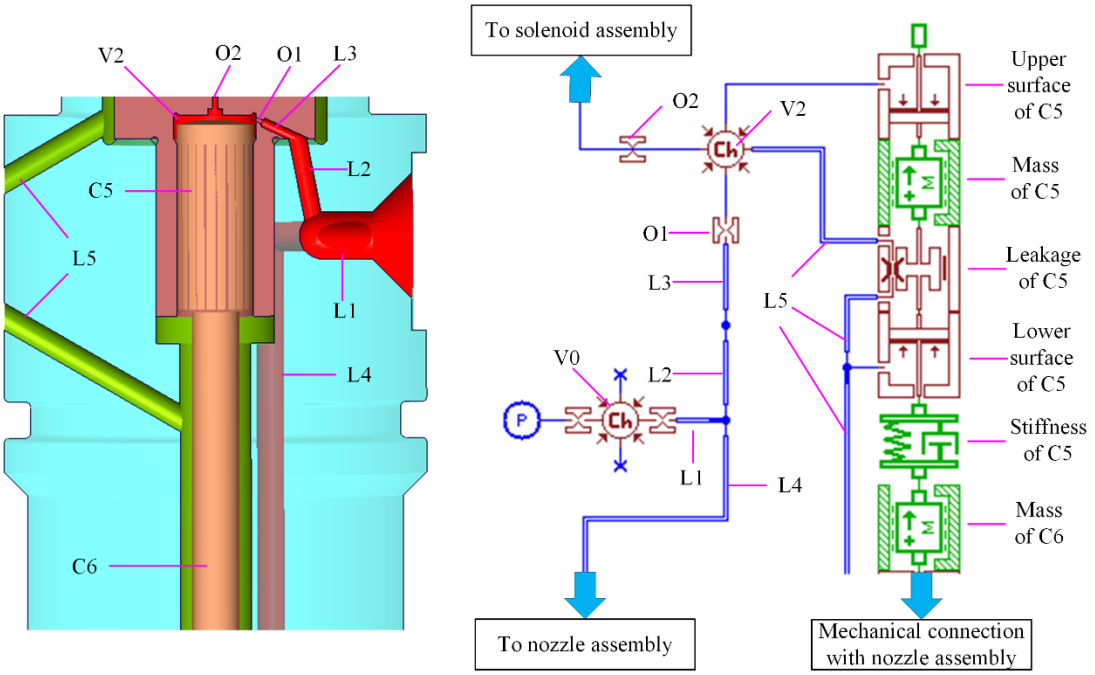


Fig. 3 Modelling of the injector body

Table 3 Parameters for the injector body

| Element | Length | Diameter | Spring rate | Dumping rate | Volume | Mass |
|---|---|---|---|---|---|---|

| | (mm) | (mm) | (N/m) | (N/(m/s)) | ($cm^3$) | (g) |
|---|---|---|---|---|---|---|
| V2 | - | - | - | - | 0.024 | - |
| O2 | - | 0.45 | - | - | - | - |
| O1 | - | 0.3 | - | - | - | - |
| L3 | 2.55 | 0.8 | - | - | - | - |
| L2 | 6.32 | 1.5 | - | - | - | - |
| C5 | 12.5 | 6.5 | 4e+8 | 400 | - | 6.4 |
| L1 | 4.2 | 4 | - | - | - | - |
| L5 | - | - | - | -- | - | - |
| L4 | 94.6 | 2.3 | - | - | - | - |
| C6 | - | - | - | - | - | 6.4 |

### 3.3 Modelling of the nozzle assembly

Fig. 4 shows a cross-sectional view of the nozzle assembly and its model, where C7 is the needle valve spring, C8 is the needle valve body, and C9 is the nozzle. V3 is the return oil chamber while V4 is the accumulation chamber. L4 is the inlet of the high-pressure fuel to the accumulation chamber V4. The nozzle assembly connects to the injector body both hydraulically and mechanically. The needle valve stiffness and mass are considered in the modelling and simulation. A piston model from AMESim is used to simulate the hydraulic force acting on the lower part of the needle valve in the accumulation chamber. The most import parts in the modelling of the nozzle assembly are the nozzle orifice parameters and their layout. Here, the group of parameters should be set accurately, for example, the needle valve diameter, the valve seat angle, the needle cone angle, the sac volume, the maximum flow coefficient of the orifices and the number of orifices.

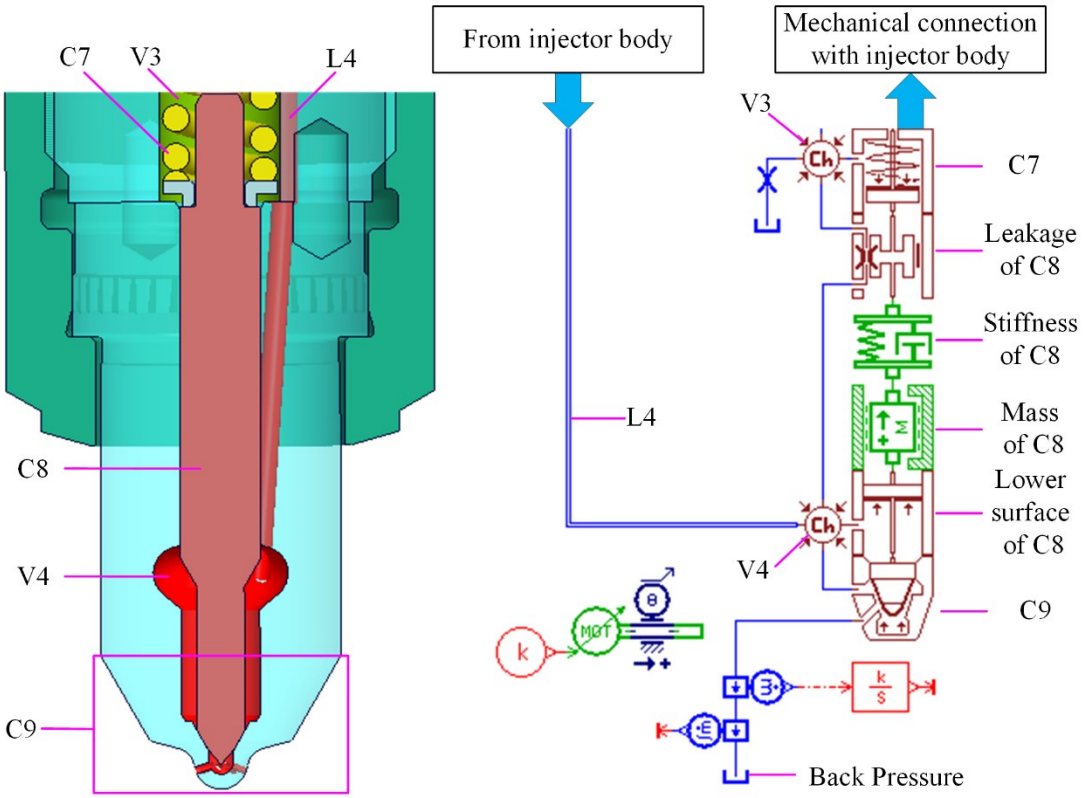


181

182 Fig. 4 Modelling of injector nozzle assembly

183 Table 4 Parameters for the injector nozzle assembly

| Element | Orifice number | Diameter (mm) | Spring rate (N/m) | Dumping rate (N/(m/s)) | Volume ($cm^3$) | Mass (g) |
|---|---|---|---|---|---|---|
| V3 | - | - | - | - | 0.2 | - |
| C7 | - | - | 13000 | - | - | 2.58 |
| C8 | - | - | 4e+8 | 400 | - | 8.6 |
| V4 | - | - | - | - | 0.348 | - |
| C9 | 9 | 0.27 | - | - | - | - |

184 **3.4 Integration of the injector model**

185 A complete sketch of the injector model is shown in Fig. 5. It is the integration of the
186 solenoid assembly, injector body and the nozzle assembly. In this model, some
187 assumptions were made that all the variations are considered to be isothermal, so, the
188 fuel temperature was assumed to be constant along the injector and equal to the one at

189 the injector inlet, and the fuel properties were assumed to be constant [26]. Additionally,
190 a constant pressure source was adopted here to simulate the pressure from the high-
191 pressure pump, which neglected the pressure fluctuations caused by the cyclical oil
192 supply from high-pressure pumps. Moreover, the pressure wave propagation was not
193 considered in the model too.

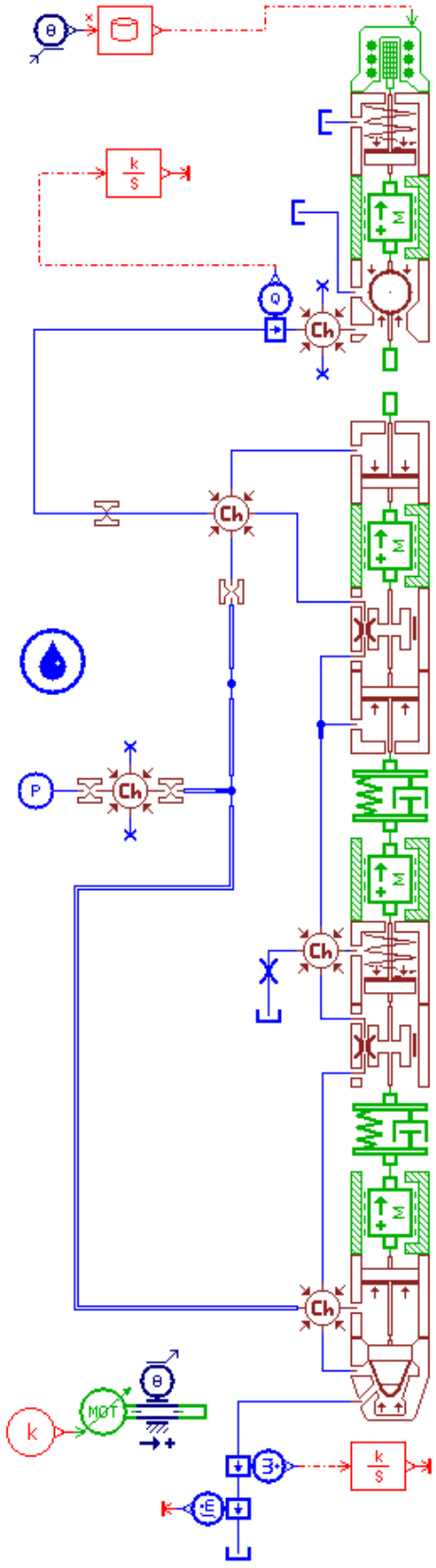


194

195 Fig. 5 Complete sketch of the electronic fuel injector model

# 4 Model validation

## 4.1 Fuel properties

A common used #0 diesel fuel in China was used in the study, the main properties are shown in Table 5.

Table 5 Physical and chemical properties of the #0 diesel fuel

| Properties | Value |
|---|---|
| Density at 20 ℃, kg/m$^3$ | 845 |
| Viscosity at 20 ℃, mm$^2$/s | 4.72 |
| Cetane number | 57.6 |
| 50% distillate at, ℃ | 273 |
| 90% distillate at, ℃ | 339 |
| 95% distillate at, ℃ | 355 |

## 4.2 Experimental facilities

The experiments were carried out on a HIL test rig. HIL is a kind of technology for semi-physical simulation, where some components in the loop are replaced by software models. The sketch of the HIL test rig is shown in Fig 6, in which the authentic diesel engine was replaced by a diesel engine model built in LABCAR system. Its working principle is shown as follows:

(1) A PID method is adopted to speed governing, i.e., the cycle injection quantity (⑥) is obtained in the ECU (⑤) by comparing the speed calculated from the camshaft

signal (⑭) and crankshaft signal (⑮) with a given speed.

(2) The width of the control signal (⑧) to fuel injectors is decided by the cycle injection quantity.

(3) Rail pressure (⑬) value is obtained by the ECU and is set as one of the input parameters to the diesel engine model. The feeding pumps of the common rail system are controlled by proportional valves to match the fuel quantity ejected.

(4) Engine speed is calculated in the diesel model by combining the cycle injection quantity (⑥) and load settings (③). This engine speed is transformed into signals to control the servo motor, which drives the camshaft (⑳) to simulate the engine running.

(5) All of the signals including temperatures, pressures and I/O status are monitored through the Compact RIO (②) and displayed in the computer (①).

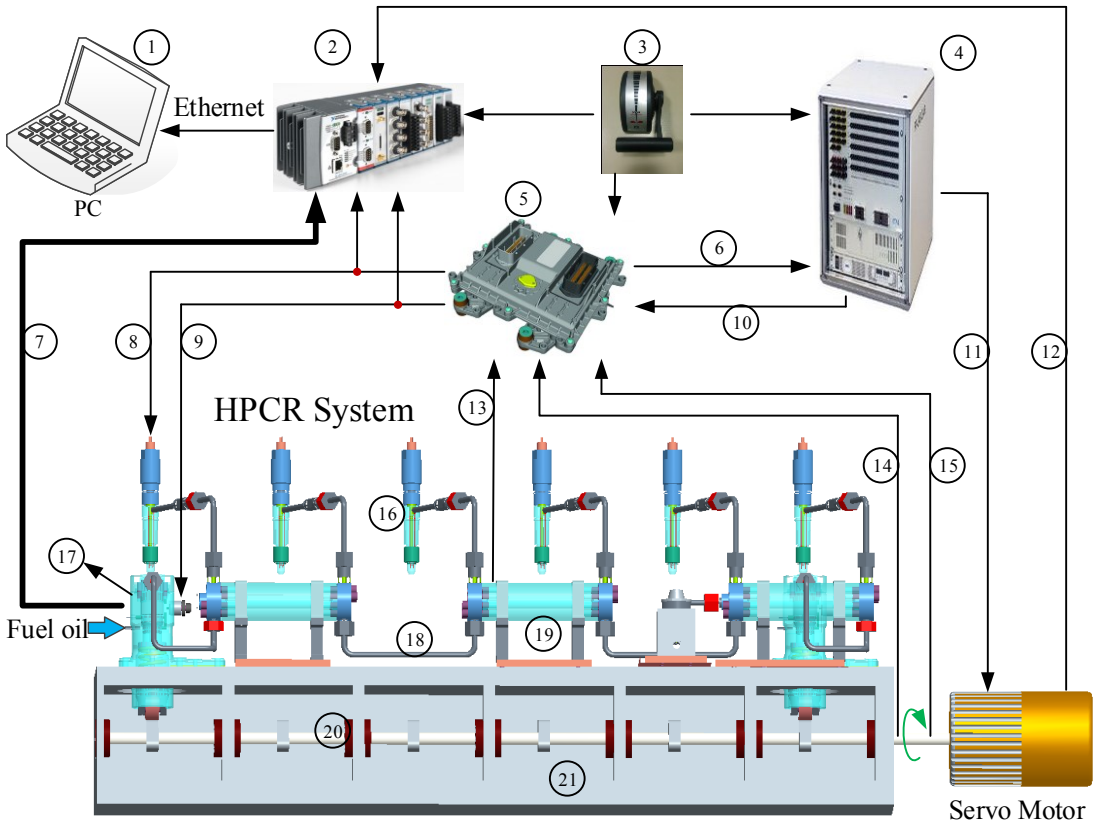


① : computer; ② : Compact RIO (a real-time embedded industrial controller made by National Instruments); ③: engine telegraph; ④: LABCAR system (a flexible test system developed by ETAS ); ⑤: ECU; ⑥: cycle fuel injection quantity; ⑦: sensor signals of the HPCR system; ⑧: ECU injection signal; ⑨: ECU control signal for the proportional valve; ⑩: correction signal from the LABCAR; ⑪: control signal for the servo motor; ⑫: encoder speed signal; ⑬: pressure signal of rails; ⑭: camshaft angle signal; ⑮: crankshaft angle signal; ⑯: injector; ⑰: high pressure pump; ⑱: high pressure oil tub; ⑲: common rail; ⑳: camshaft; ㉑: oil pan.

Fig. 6 Systematic configuration of the HIL test rig

### 4.1.2 Injection quantity measuring

One of the most important parts of the HIL test rig would be the injection quantity measuring device. The sketch of it is shown in Fig. 7. Oil injected from the injector (①) flows through the demister (②) and cooler (④) successively, then flows to the oil weighting device. Two weighting methods are available, one measures the fuel volume via a measuring glass (⑧), the other weights the fuel mass via an electronic scale (⑨).

The two methods can be switched to each other in the control of a PLC (⑫) through an electronic three-way valve (⑤).

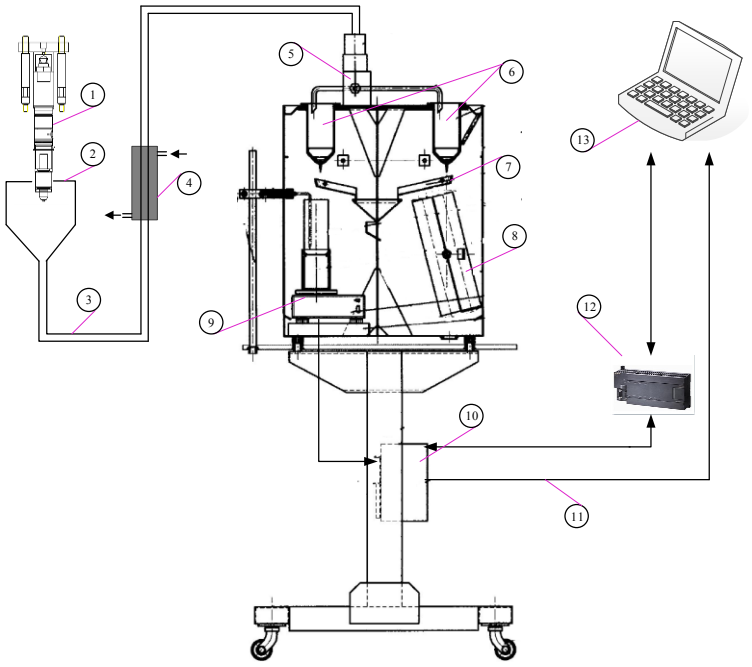


①: electronic fuel injector; ②: demister; ③: oil tube; ④: cooler; ⑤: three-way valve; ⑥: collector; ⑦: oil baffle plate; ⑧: measuring glass; ⑨: electronic scale; ⑩: junction box; ⑪: cables; ⑫: PLC.

Fig. 7 Fuel oil measurement device

## 4.3 Validation

Limited by the experimental conditions, only the injection quantity data could be obtained for validating the electronic fuel injector model from the HIL test rig. Experiments were carried out at room temperature and under 4 different rail pressures, i.e., 80 MPa, 100 Mpa, 120 MPa and 140 MPa. Under each pressure, 4 different fuel injection pulse widths were applied, i.e., 1ms, 1.5ms, 2ms and 2.5ms. The injection mass comparison of simulation results and experimental results are shown in Fig. 8. The average steady-state mass flow rate calculated by the injection quantity data are

compared with simulation fuel injection rate, as is shown in Fig. 9. The average steady-state mass flow rate of the 1ms injection pulse condition is excluded since it is too short for the injection rate to reach a steady state. The average steady-state mass flow rates of 1.5ms, 2.0ms and 2.5ms under different pressures are represented by red circles, red triangles and red squares respectively.

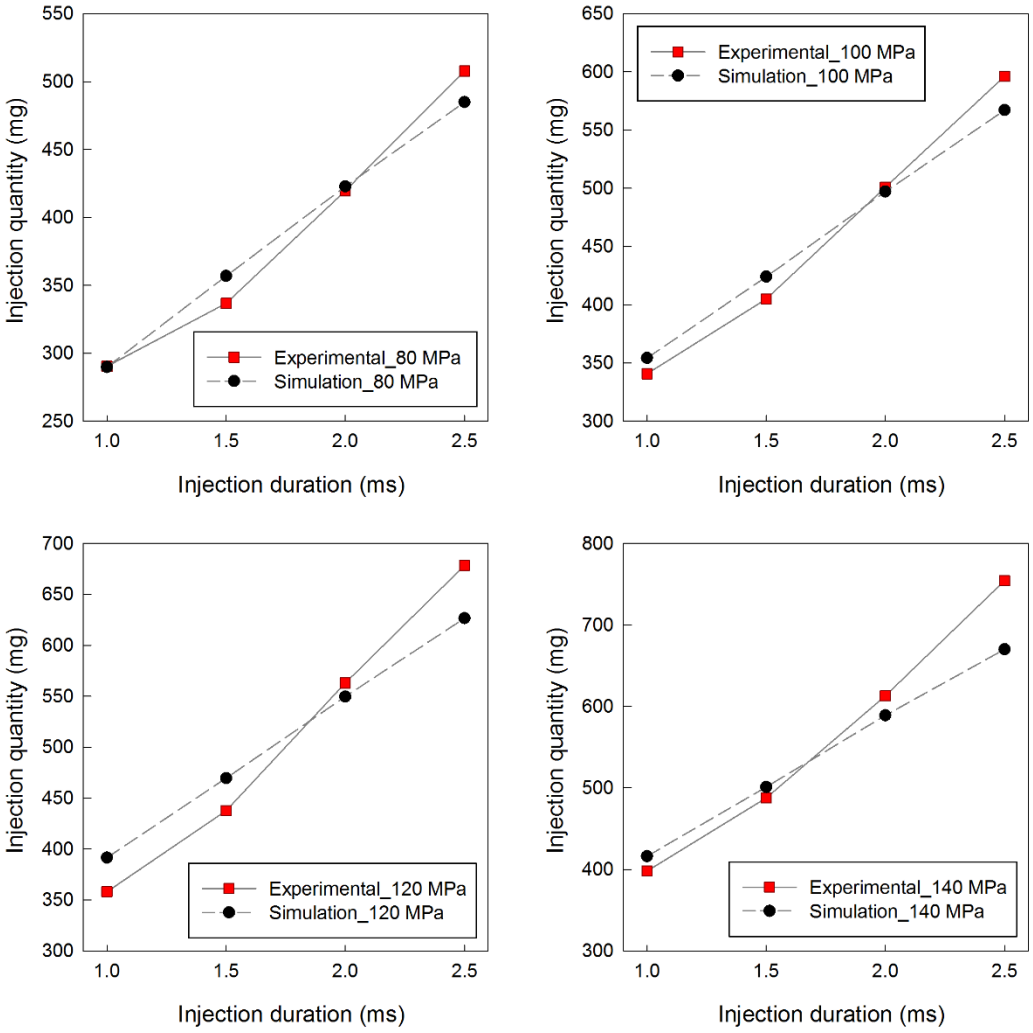


Fig. 8 Injection mass comparisons of experimental data and simulation data

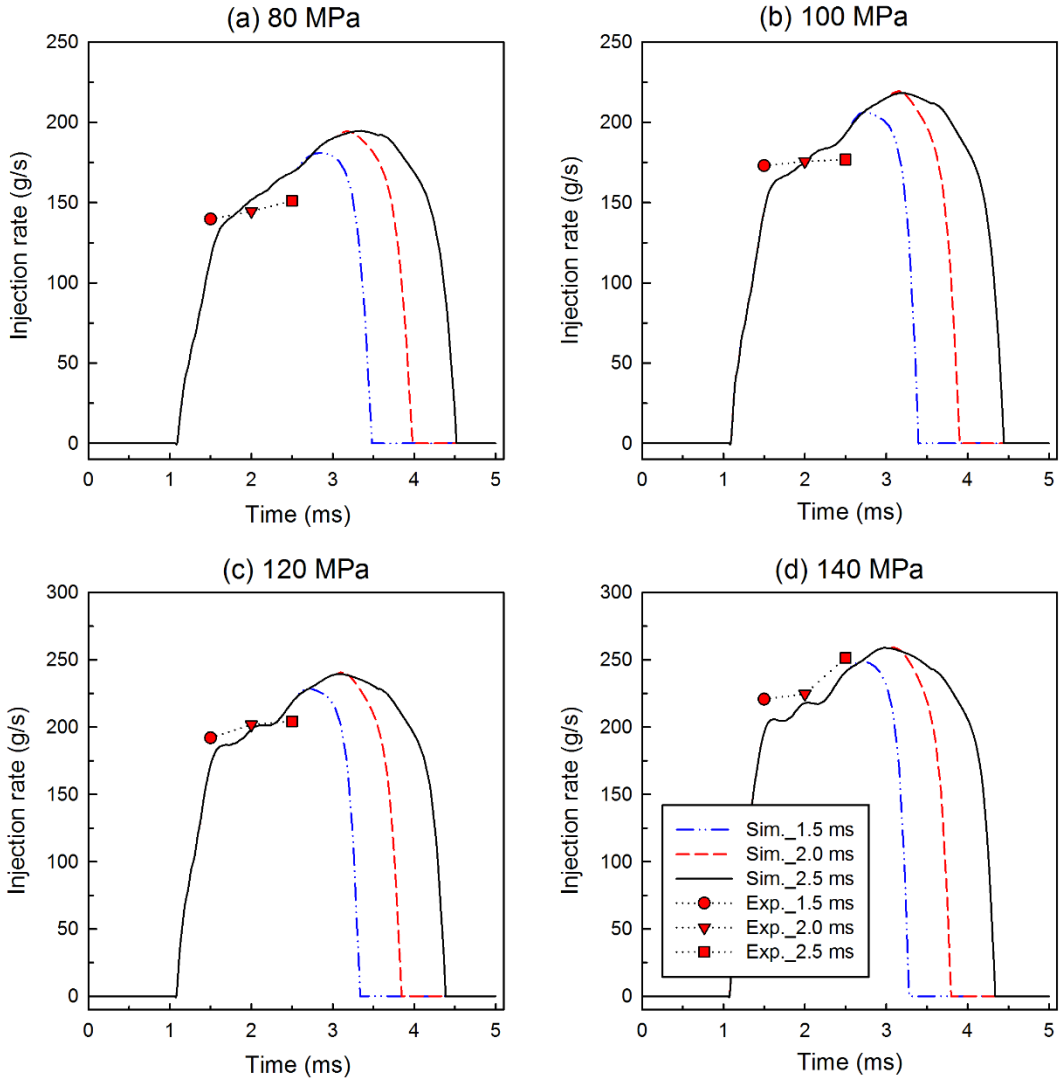


257

258 Fig. 9 Average steady flow rate comparison of experimental data and simulation data

259 It can be seen that the main trend in simulation data for total injection mass and average

260 steady-state mass flow rates show agreement with the experiment data under all four

261 different rail pressures.

262 # 5 Multi-objective optimisation of the electronic fuel injector

263 ## 5.1 Definition of the optimisation objectives

264 The details of the objective definition are shown in Fig. 10, where the opening delay is

265 defined to Δ T1, which is the delay between t1 and T2, and the closing delay is defined
266 to Δ T3, which is the delay between t3 and T4. In other words, Δ T1=T2-t1 and Δ T3=
267 T4-t3. A small opening delay and closing delay mean that a faster and better response
268 can be achieved which offers greater flexibility for developing multi-injection control
269 strategies. Thus, the opening delay and the closing delay are set as the two objectives
270 to be minimised.

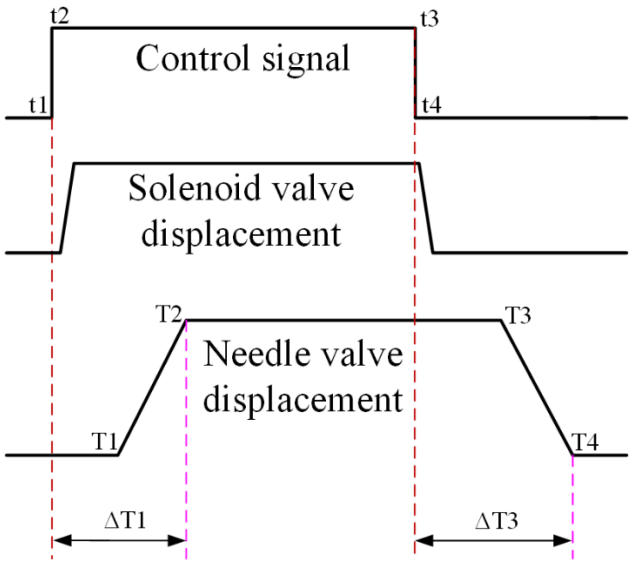


271
272 t1: the control signal starts to be energised; t2: the control signal has reached to its maximum amplitude;
273 t3: the control signal begins to be de-activated; t4: the control signal has fully closed; T1: the needle
274 valve starts to open; T2: the needle valve has reached its maximum displacement; T3: the needle valve
275 begins to close; T4: the needle valve has fully closed.

276 Fig. 10 Definition of the dynamic response

277 **5.2 Optimisation model**

278 An optimisation model was built within the modeFRONTIER software for multi-
279 objective optimisation, as is shown in Fig. 11. Firstly, a random sequence was adopted
280 in the DOE type. Then, an NSGA-II algorithm was selected. After that, a MATLAB
281 node containing a program for setting the nozzle diameters according to the nozzle

orifice number was created. An AMESim node was used to invoke the whole electronic fuel injector model, where the displacements of the control signal and the needle valve were generated. These data was firstly written into a text file, and to do this, appropriate writing and reading rules needed to be developed. The text file is read by the MATLAB node, where the control signal timings (t1, t2, t3 and t4) and needle valve lift timings (T1, T2, T3 and T4) are calculated. The opening delay and the closing delay can thus be obtained from the timings according to the definition shown in section 5.1. Additionally, a constraint was set between the fuel oil inlet passage diameter and fuel oil outlet passage diameter that the former should be smaller than the latter in each run.

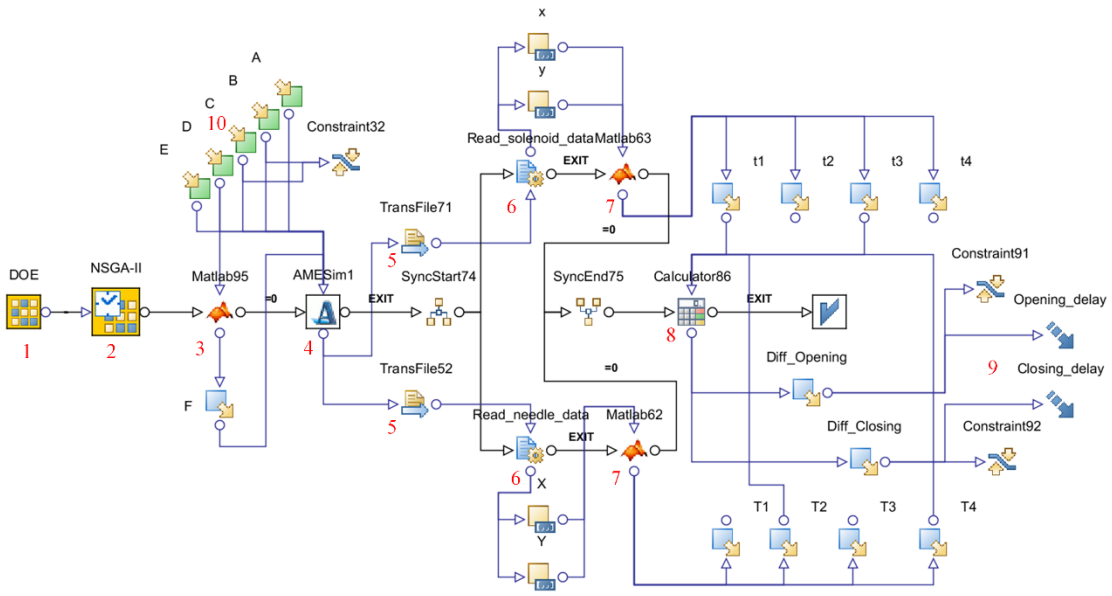


1: DOE type; 2: MOGA Algorithm; 3: MATLAB node; 4: AMESim node; 5: transfer the text files of the control signal and the needle valve displacement synchronously; 6: read the control signal data and the needle valve displacement data from files respectively; 7: MATLAB node; 8: calculation of the objectives; 9: objectives; 10: input parameters.

Fig. 11 Multi-objective optimisation model

## 5.3 Boundaries and settings of input parameters

The boundaries and resolutions of input parameters are specified in Table 6. References

for setting boundaries in the optimisation were obtained from parametric study.

Table 6 Input parameters of the multi-objective optimisation model

| Input parameter | Lower bound | Upper bound | Resolution |
|---|---|---|---|
| CPD (mm) | 5.8 | 8.0 | 0.1 |
| IPD (mm) | 0.2 | 0.45 | 0.01 |
| OPD (mm) | 0.36 | 0.9 | 0.02 |
| NZN | 6 | 10 | 1 |
| SPF (N) | 60 | 360 | 10 |

The range of nozzle orifice diameter (NZD) is set according to the parameter NZN, as shown in Fig. 12. The parameter NZD under each NZN can be set to five values, which are chosen randomly in the MATLAB node. Thus, an approximate total circulating area of the fuel injector nozzle is guaranteed.

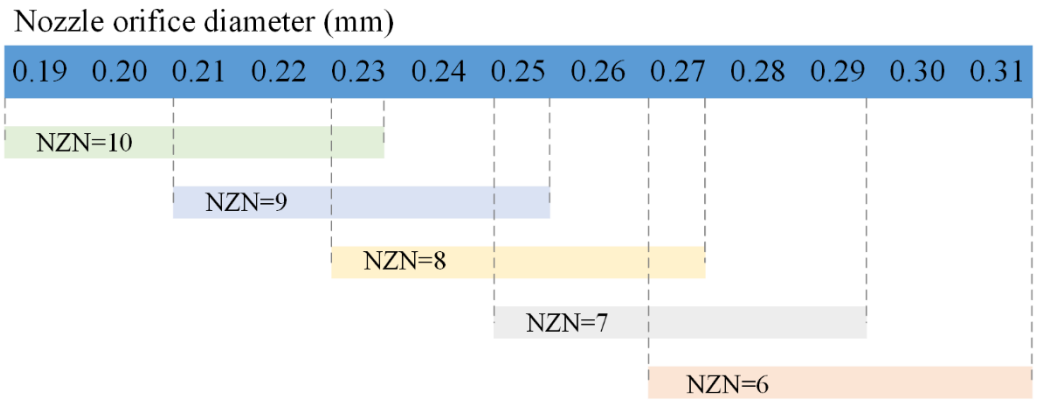


Fig. 12 The range of the NZD under various values of the NZN

## 5.4 Calculation settings

Table 7 gives detailed information about the calculation settings for the NSGA-II method. The 100 initial random DOE designs were each coordinated with 20 generations runs [27]. Thus, a total number of 2000 runs were carried out. In theory, the larger the numbers, the closer the optimal designs to the real Pareto frontier. Other parameters were set as default values in the modeFRONTIER [28].

Table 7 Calculation settings for the NSGA-II algorithm

| Property | Value |
|---|---|
| Number of initial designs | 100 |
| DOE scheme | RANDOM |
| Optimization algorithm | NSGA-II |
| Number of generations runs | 20 |
| Crossover probability | 0.9 |
| Mutation probability for real-coded vectors | 1.0 |
| Mutation probability for binary strings | 1.0 |
| Crossover type for binary-Code variables | Simple |
| Total number of analyses | 2000 |

# 6 Results and discussion

## 6.1 Influential factors analysis

The importance of structural parameters and their interactions to the objectives were studied through a second order Smoothing Spline Analysis of Variance (ANOVA) algorithm. Here, structural parameters and their interactions are referred to factors. The relative importance ranking is shown in Fig. 13. All of the weights of factors add up to 1 and only the top six influential factors are reported in the figure. The left column and the right column show the relative importance of factors on the opening delay and closing delay respectively. The first row, the second row and the third row demonstrate the results under the rail pressures of 80 MPa, 120 MPa and 160 MPa respectively.

The left column of Fig.13 indicates that parameters CPD, IPD, OPD and their interactions are the most influential factors on the opening delay of all the three rail pressures. Although the CPD, IPD and their interactions rank as the first three factors, other factors such as the OPD, interactions of the CPD&IPD and IPD&OPD are still not negligible. The right column of Fig. 13 shows that the IPD has a dominant influence on the closing delay, which is nearly two to three times larger than CPD, which is the second largest influential factor. The influences of the NZN and NZO on dynamic response are much less than the IPD and CPD have.

The effects of these important influential factors on the dynamic response were

demonstrated by RSM function charts at 160 MPa pressure, which is shown in Fig. 14. These function charts were generated through the RSM function on selected parameters. Only one parameter is changed at a time while other parameters are kept at the same values as the baseline design. Thus, the way in which these important parameters affect the opening delay and closing delay can be easily seen. It can be seen in Fig. 14 that the increase in CPD and IPD leads to a huge rise in the opening delay. However, the increase in OPD reduces the opening delay. As for the closing delay, this decreases with an increase in parameters IPD and SP. When the CPD increases, the closing delay drops accordingly.

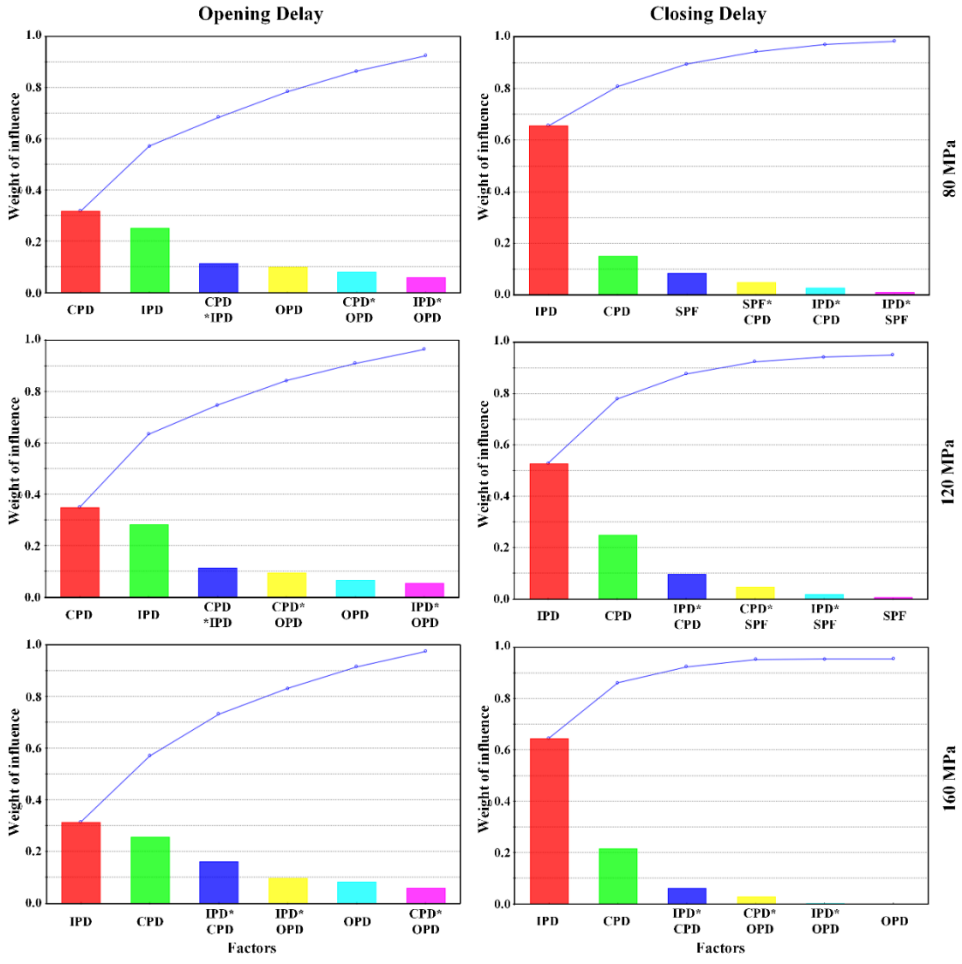

Fig. 13 Importance rank of structural parameters to objectives

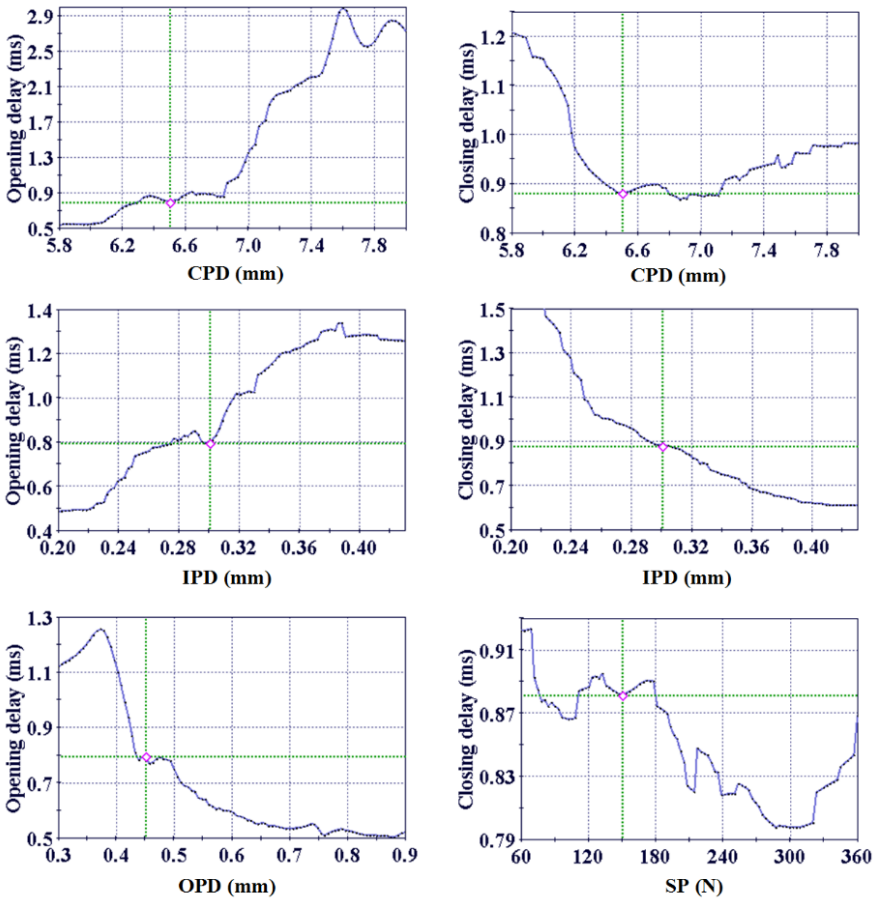


Fig. 14 RSM function charts at 160 MPa rail pressure

The CPD mainly affects the upper surface area of the control piston. Thus, a larger CPD means a larger upper surface area of the control piston, and a larger pressure force being exerted on it. Since the pressure force working on the lower part of the needle valve remains the same, a smaller net force is obtained when the solenoid valve is energised. However, it is exactly this net force pushes the needle valve upward to start the fuel injection. In this condition, the smaller net force surely slows down the needle valve opening velocity, and conversely, extends the opening delay. When the solenoid valve

358 is deactivated, the control chamber regains rail pressure and a larger opposite net force
359 pushes the needle valve downwards quickly, which reduces the closing delay. However,
360 the influence of CPD on the closing delay is much smaller than that on the opening
361 delay, proofs can be seen in the first row of Fig. 14.
362
363 The IPD mainly affects the oil charge rate. A larger IPD brings in a bigger oil charge
364 rate when the solenoid valve is energised. Since the oil discharge rate in the oil outlet
365 passage remains the same, the pressure in the control chamber drops slower than with
366 a small IPD, which slows down the opening velocity at the opening stage and
367 accelerates the needle valve closing velocity at the closing stage. Thus a larger IPD
368 leads to a larger opening delay and a smaller closing delay and vice versa. Proof can be
369 seen in the second row of Fig. 14.
370
371 An interesting phenomenon can be seen from the left column of Fig. 13 that the CPD
372 is the most influential factor in the opening delay at 80 MPa pressure and 120 MPa
373 pressure but its position is replaced by the IPD at 160 MPa pressure. As it is already
374 presented, the CPD affects the area on which the pressure exerts and the IPD affects the
375 fuel oil charge rate of the control chamber. Both of them affects the pressure force on
376 the upper surface of the control piston eventually. At high-pressure condition, a larger
377 oil charge rate can be seen than that at low-pressure condition, even the IPD remains
378 the same. This is the main reason for a more import role the IPD plays at high-pressure
379 condition. Another attracting phenomenon that the CPD is relevant to the closing delay

380 at low-pressure condition, and the relevance decreases at medium pressure and it
381 increases again at high-pressure condition, as shown in the right column of Fig. 13. The
382 possible reasons which caused this might be the different samples used for the analysis
383 since these different samples were generated by three different runs under three
384 different pressures.
385
386 The OPD determines the oil discharge rate. A larger OPD means more fuel can be
387 discharged from the control chamber into the low-pressure chamber if other conditions
388 are kept the same. Thus, the pressure force exerted on the upper surfaces of the control
389 piston decreases quickly to help the needle valve open. In this case, a smaller opening
390 delay is achieved.
391
392 From the third row of Fig. 14, it can be seen that the closing delay decreases with the
393 increase in SPF. It can be easily construed that a larger SPF helps the needle valve move
394 upwards faster. In other words, a larger SPF increases the downward net force so that
395 the movement of the needle valve is accelerated to shorten the closing delay. From the
396 right column of Fig. 13, the SPF is surprisingly influential on objectives at low-pressure
397 condition but its influence diminishes at high-pressure condition. At low-pressure
398 condition, the pressure forces exerting on the upper surface of the control piston and on
399 the lower part of the needle valve are both smaller than that at high-pressure condition.
400 Since the SPF remained the same, thus, the rates of the SPF to the pressure forces at
401 low-pressure condition are larger than that at high-pressure condition. Therefore, the

SPF is more comparable to the small hydraulic forces at low-pressure condition, however, it becomes ignorable to the large hydraulic forces when the pressure increases.

### 6.2 Response surface analysis

Fig. 13 highlights the fact that factors CPD, IPD and their interactions are of greatest significance to the opening delay and the closing delay. Since the response surfaces at 80 MPa and 120 MPa are nearly the same as that at 160 MPa, only the response surface at 160 MPa was generated and demonstrated. The RSM contour maps are shown in Fig. 15 and Fig. 16. In both figures, the bright points present the performance of the baseline design.

From Fig. 15, it can be clearly seen that a small CPD together with a small IPD contributes to a short opening delay. However, large CPD and IPD increase the opening delay dramatically. As it is stated in section 6.1, a large CPD diminishes the net force which pushes the needle valve moving upward and enlarges the opening delay. This is especially true when large IPD applied, which slows down the pressure drop in the control chamber to help increase the opening delay.

Fig. 16 shows that a small closing delay is achieved with a large IPD. A small CPD and a small IPD together lead to a significant increase in the closing delay. A small IPD decreases the fuel oil charge rate so that the control chamber needs longer time to regain

the rail pressure. Thus, a larger closing delay comes along. Combine with a small CPD, which weakens the net force pushing needle valve downward, an extreme longer closing delay shows up.

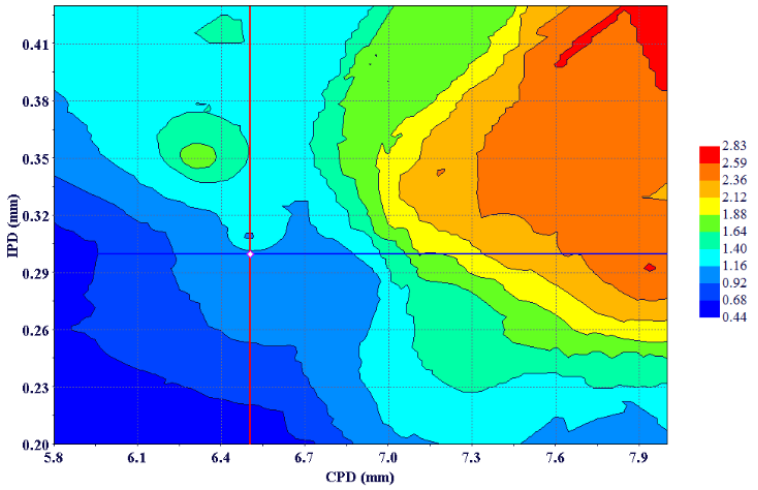


Fig. 15 Response surface of the opening delay under 160 MPa rail pressure

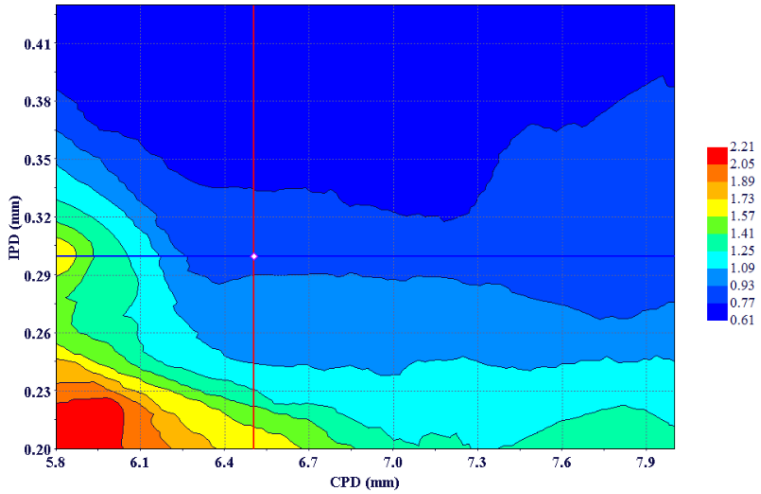


Fig. 16 Response surface of the closing delay under 160 MPa rail pressure

## 6.3 Pareto optimum

Fig. 17 (a), (b) and (c) are the optimisation results for three different rail pressures (80 MPa, 120 MPa and 160 MPa respectively). The Pareto citizens are marked with black

solid triangles. The baseline design is marked with a deep blue square and the selected optimal design is shown as a green hollow reversed triangle.

A clear trade-off can be seen between the opening delay and the closing delay in each figure. Pareto frontiers are also noted to be closer to the coordinates under a high rail pressure than under a low rail pressure. This indicates that a high pressure contributes to faster opening and closing movements of the electronic fuel injector, and thus to a shorter opening delay and closing delay.

Table 8 gives the detailed improvements of the selected optimal design. Compared to the baseline design, both the opening delay and the closing delay of the selected optimal design have witnessed a huge reduction in all three rail pressures, specifically, the reduction of 29.82%, 29.19% and 20.86% in the opening delay at pressures of 80 MPa, 120 MPa and 160 MPa respectively. Nearly the same reduction scale, i.e., 25.62%, 24.54% and 30.11% for the closing delay was achieved under different pressures respectively. Table 8 shows the specific values of the opening delays and closing delay of the optimal design and the baseline design, and comparisons are made in Fig. 18. Table 9 reports the structural parameter details of the baseline design and the optimal design.

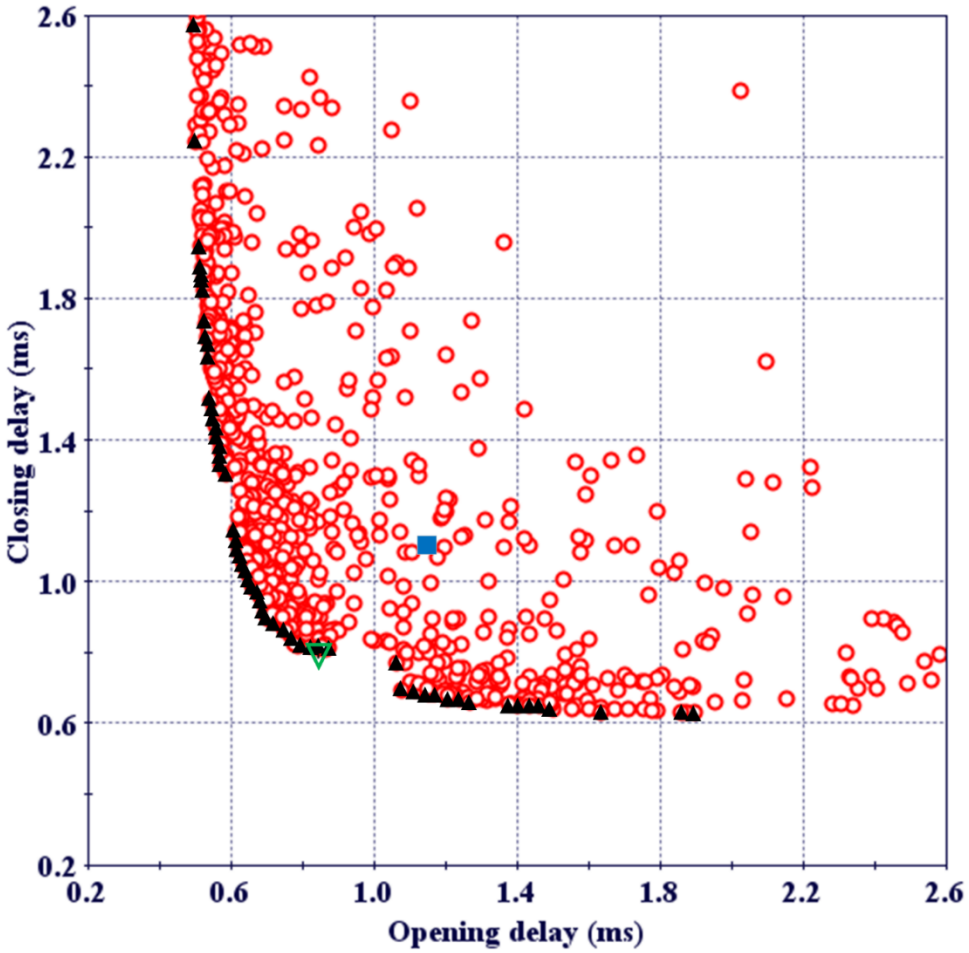


454

455 (a) Scattering results under 80 MPa rail pressure

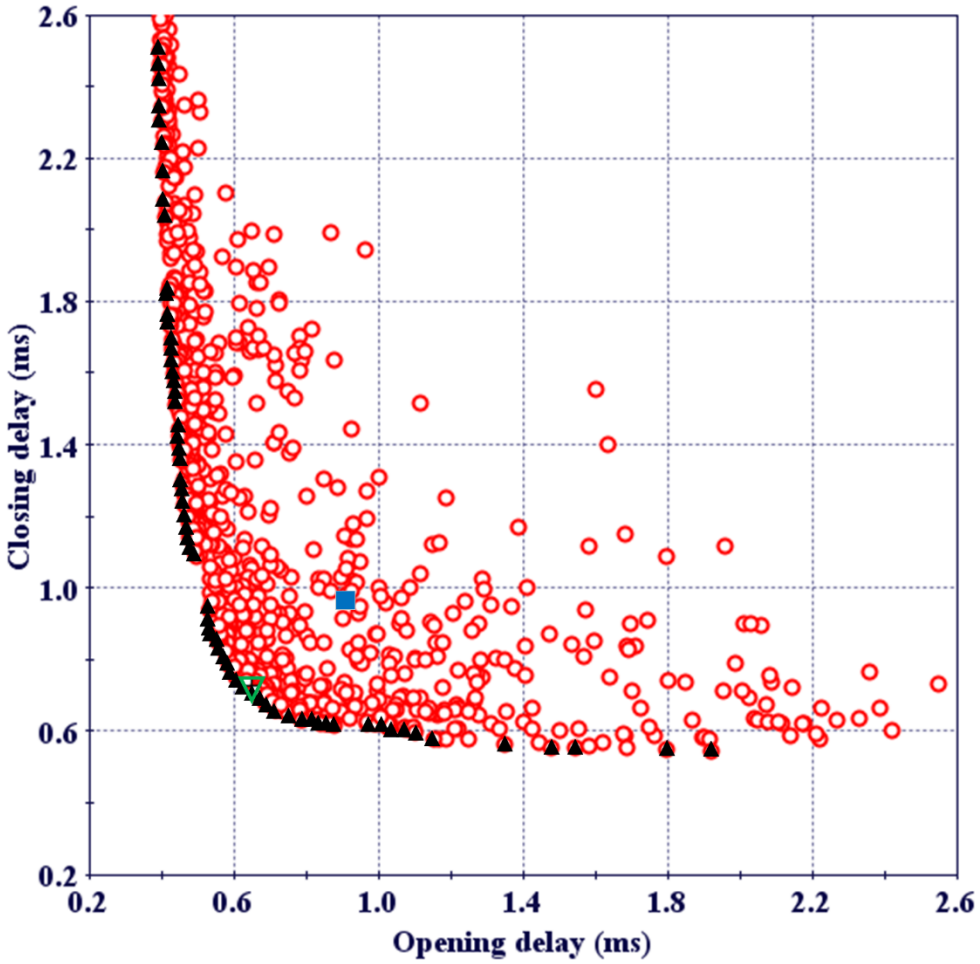


456

457 (b) Scattering results under 120 MPa rail pressure

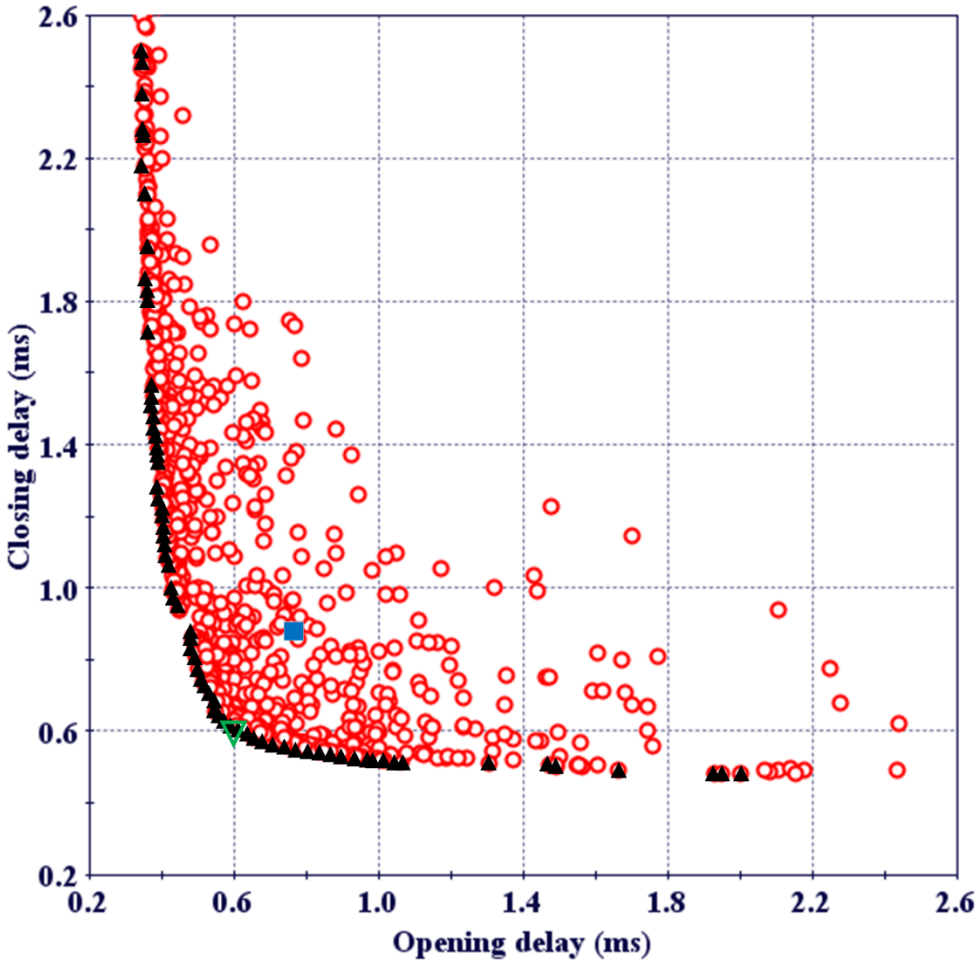


458

459 (c) Scattering results under 160 MPa rail pressure

460 Fig. 17 Pareto citizens and the selected designs under various rail pressures

461

462 Table 8 Detailed objective comparisons of the optimal design and the baseline design

| Pressure (MPa) | Delay | Baseline (ms) | Optimum (ms) | Status | Degree （%） |
|---|---|---|---|---|---|
| 80 | Opening | 1.197 | 0.840 | ↓ | 29.82 |
| | Closing | 1.097 | 0.816 | ↓ | 25.62 |

| | | | | | |
|---|---|---|---|---|---|
| 120 | Opening | 0.908 | 0.643 | ↓ | 29.19 |
| | Closing | 0.974 | 0.735 | ↓ | 24.54 |
| 160 | Opening | 0.767 | 0.607 | ↓ | 20.86 |
| | Closing | 0.880 | 0.615 | ↓ | 30.11 |

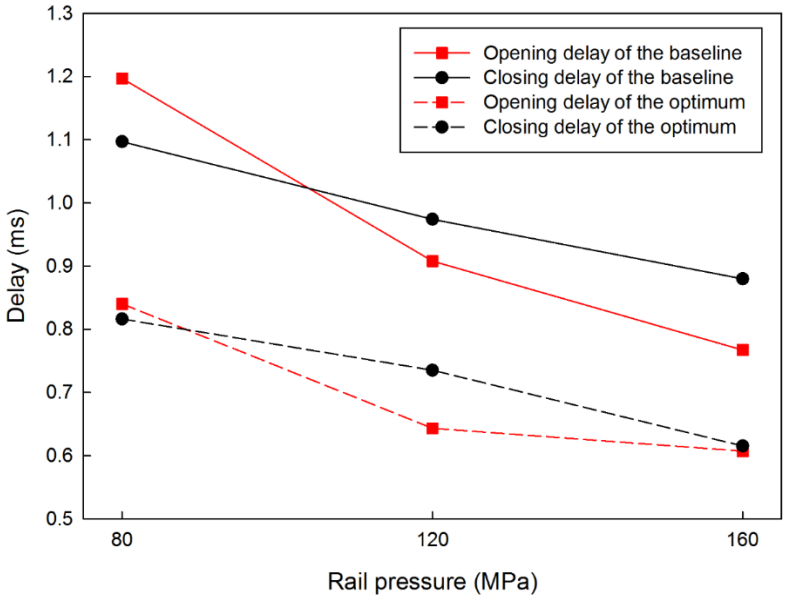


463

464 Fig. 18 Objective comparisons of the baseline design and the optimal design

465

466 Table 9 Comparison of structure parameter values before and after optimisation

| Parameter | Baseline | Optimum |
|---|---|---|
| CPD (mm) | 6.5 | 6.2 |
| IPD (mm) | 0.3 | 0.39 |
| OPD (mm) | 0.45 | 0.90 |
| NZN | 9 | 9 |

| | | |
|---|---|---|
| NZD (mm) | 0.27 | 0.23 |
| SPF (N) | 149 | 290 |

Since the selected optimal design reaches the maximum value of the OPD, which implies the upper bound for the OPD might be set too small. Thus, a further study on the OPD was carried out to examine the effects of it on injector dynamic response independently at the three rail pressures respectively. Results are shown in Fig. 19 that the closing delay remained almost the same while the opening delay decreases monotonously with the increases of the OPD but the trend becomes gentle, especially when the OPD is larger than 0.9mm. In this manner, enlarge the upper bound of the OPD would be meaningless.

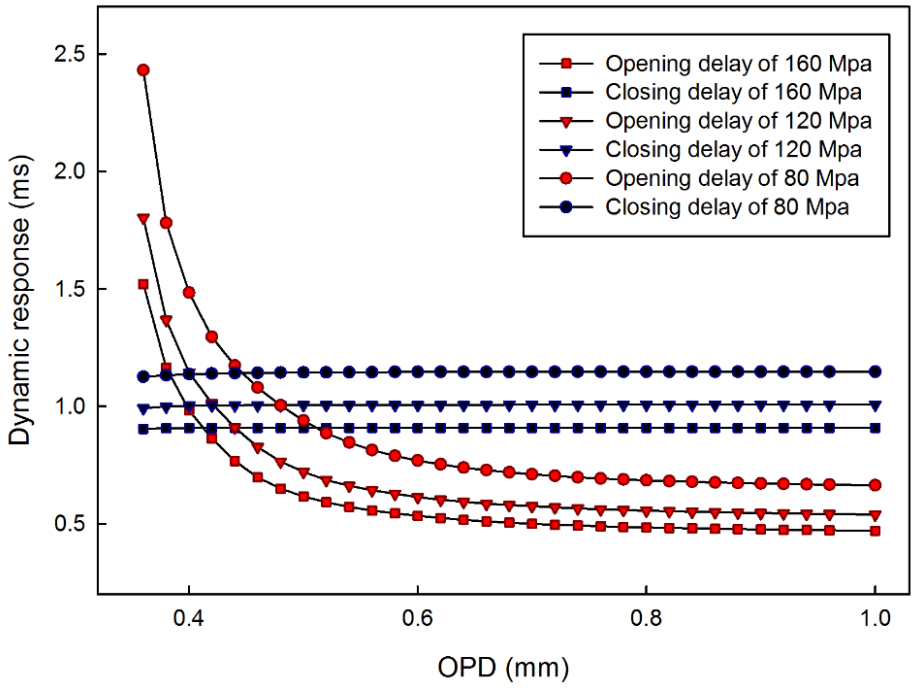


Fig. 19 The effect of OPD on injector dynamic response

The solenoid valve displacement and needle valve displacements of both the baseline design and the optimal design are compared for three different rail pressures, as shown in Fig. 20. The injection rate is shown in Fig. 21. In both figures, the needle valve displacements of the baseline design under different rail pressures are represented by black lines, while needle valve displacements of the optimum under various rail pressures are shown by red ones. Different rail pressures are distinguished by line types, i.e., 160 MPa, 120MPa and 80MPa are represented by solid lines, dash lines and dot lines respectively. The control signal, marked by blue lines, are also drawn in both the Fig. 20 and Fig. 21 in order to have references. Since the nozzle orifice diameter of the optimal deign is smaller than that of the baseline design, the maximum injection rate is much less under the same energise time, as shown in Fig. 21.

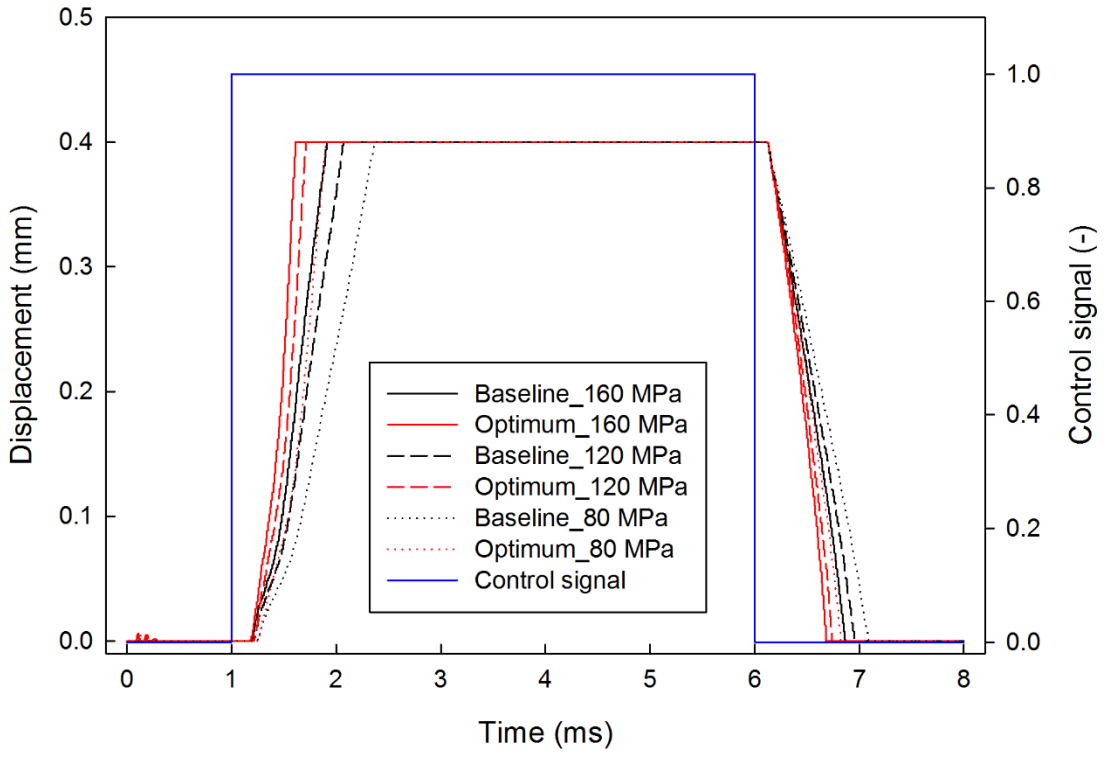


Fig. 20 Needle valve displacement comparisons of the baseline design and the selected optimum

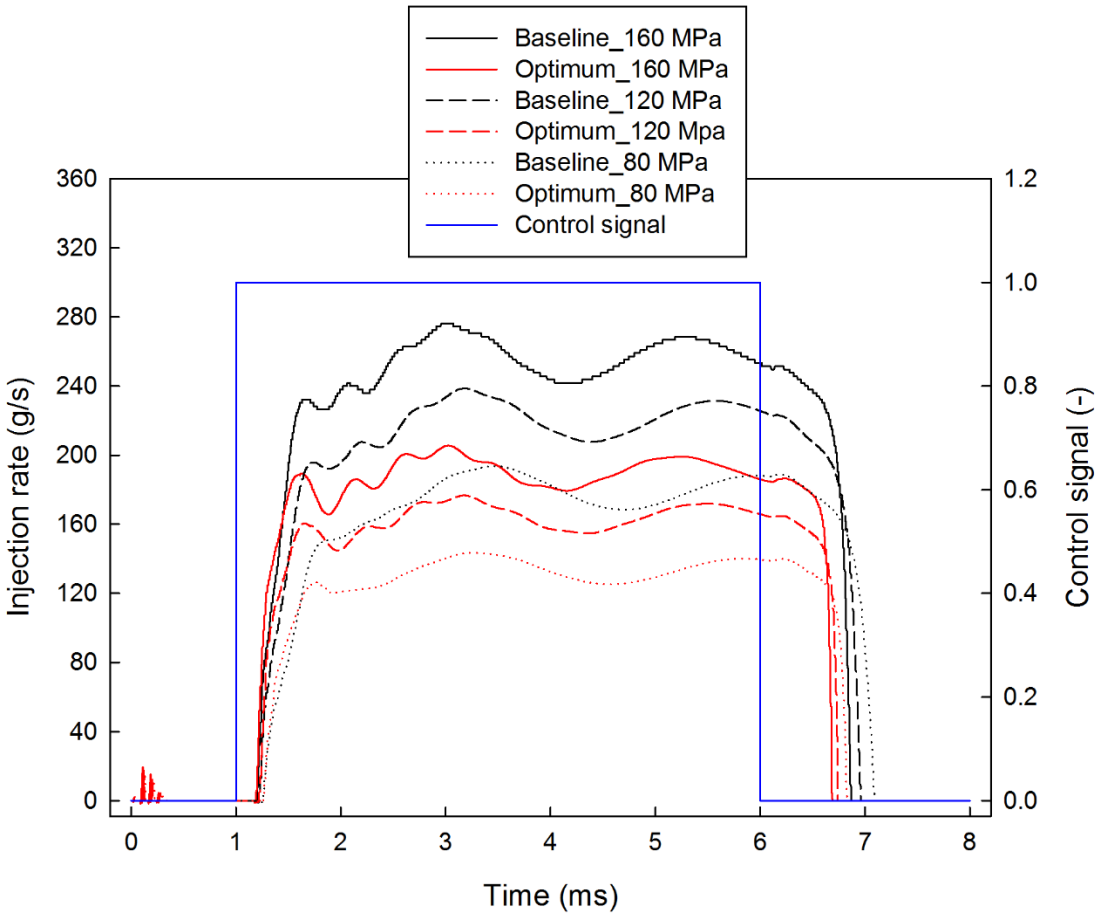


490

491 Fig. 21 Injection rate of the baseline design and the optimal design under various rail pressures

492 ## 7 Conclusion

493 The above research concentrated on the modelling and optimisation of structural
494 parameters of an electronic fuel injector. A complete and detailed model of the
495 electronic fuel injector was built using AMESim software according to its physical
496 geometries. The model was validated by the experimental injection quantity data and
497 average steady-state mass flow rate (if test condition permits, the injector model is
498 better to be validated by injection quantity together with transient injection rate)
499 obtained from a HIL test rig. Then, an optimisation model was built using
500 modeFRONTIER software and optimisation was carried out through the MOGA

501 method. The importance of the structural parameters of the dynamic response was
502 examined. RSM function charts disclosed how these important structural parameters
503 affect the dynamic response. Then, RSM contour maps were applied to study the
504 interactions between the CPD and IPD. Finally, a Pareto optimal design with the best
505 trade-off between the opening delay and the closing delay was singled out.
506
507 The main conclusions are drawn below:
508
509 (1) The CPD, IPD, OPD and their interactions are influential factors for the opening
510 delay, while the IPD has a dominant effect on the closing delay.
511
512 (2) The increases in the CPD and IPD lead to a huge rise of in the opening delay.
513 However, the increase in the OPD reduces the opening delay. The closing delay
514 decreases with the increase in the IPD and SP. Moreover, it drops along with the
515 increase in CPD.
516
517 (3) A small CPD together with a small IPD contribute to a short opening delay but
518 enlarge the closing delay significantly. To the opposite, a large CPD and IPD increase
519 the opening delay dramatically. A large IPD also minimises the closing delay.
520
521 (4) The effects of the spring preload force on the closing delay are surprising noticeable
522 at low rail pressure condition. The closing delay decreases with the increase of the

spring preload force.

(5) The dynamic response of the selected optimal design achieves a huge reduction in 3 different rail pressures (80 MPa, 120 MPa and 160 MPa). More specifically, the opening delay reduced by 29.82%, 29.19% and 20.86%, and the closing delay reduces by 25.62%, 24.54% and 30.11% respectively.

## Acknowledgment

The authors are grateful to the Wuhan University of Technology for providing experimental facilities and test data. We also appreciate the Department of Naval Architecture, Ocean and Marine Engineering of the University of Strathclyde for the calculation support on the project.

Funding: This work was supported by the project “Engineering Development of a Medium-Speed Dual Fuel Engine (Ministry of Industry and Information Technology NO. (2013) 412, 2)” from China and the project “An Investigation into the Characteristics of High-pressure Common Rail Injection System” from Lloyds Register of Shipping of UK.

## References

[1] Molina S, Salvador FJ, Carreres M, Jaramillo. A computational investigation on the influence of the use of elliptical orifices on the inner nozzle flow and cavitation development in diesel injector nozzles. Energy Conversion and Management 2014; 79:114-127.

[2] Benajes J, Pastor JV, Payri R, Plazas AH. Analysis of the influence of diesel nozzle geometry in the injection rate characteristics. J Fluids Eng. 2004; 126: 63-71.

[3] Payri R, Garcia JM, Salvador FJ, Gimeno J. Using spray momentum flux measurements to understand the influence of diesel nozzle geometry on spray characteristics. Fuel 2005; 84: 551-561.

[4] Han JS, Lu PH, Xie XB, Lai MC, Henein NA. Investigation of diesel spray primary breakup and development for different nozzle geometries. SAE Paper 2002; 2002-01-2775.

[5] He Z, Zhong W, Wang Q, Jiang Z, Fu Y. An investigation of transient nature of the cavitating flow in injector nozzles. Applied Thermal Engineering 2013; 54: 56-64.

[6] Moon S, Gao Y, Park S, Wang J, Kurimoto N, Nishijima Y. Effect of the number and position of nozzle holes on in- and near-nozzle dynamic characteristics of diesel injection. Fuel 2015; 150:112-122.

[7] Salvador FJ, Martínez-López J, Caballer M, De Alfonso C. Study of the influence of the needle lift on the internal flow and cavitation phenomenon in diesel injector nozzles by CFD using RANS methods. Energy Conversion and Management 2013; 66:246-256.

[8] Salvador FJ, Gimeno J, De la Morena J, Carreres M. Using one-dimensional

modeling to analyze the influence of the use of biodiesels on the dynamic behavior of solenoid-operated injectors in common rail systems: Results of the simulations and discussion. Energy Conversion and Management 2012; 54: 122-132.

[9] Wang C, Li GX, Sun ZY, et al. Effects of structure parameters on flow and cavitation characteristics within control valve of fuel injector for modern diesel engine. Energy Conversion and Management 2016; 124: 104-115.

[10] Beccari S, Pipitone E, Cammalleri M, Genchi G. Model-based optimization of injection strategies for SI engine gas injectors. Journal of Mechanical Science and Technology 2014; 28 (8): 3311-3323.

[11] Cheng Q, Zhang ZD, Xie NL. Power losses and dynamic response analysis of ultra-high speed solenoid injector within different driven strategies. Applied Thermal Engineering 2015; 91: 611-621.

[12] Salvador FJ, Gimeno J, Carreres M, Crialesi-Esposito M. Fuel temperature influence on the performance of a last generation common-rail diesel ballistic injector. Part I: Experimental mass flow rate measurements and discussion. Energy Conversion and Management 2016; 114: 364-375.

[13] Payri R, Salvador FJ, Carreres M, DelaMorena J. Fuel temperature influence on the performance of a last generation common-rail diesel ballistic injector. Part II: 1D model development, validation and analysis. Energy Conversion and Management 2016; 114: 376-391.

[14] Seykens XLJ, Somers LMT, Baert RSG. Detailed modelling of common rail fuel injection process. J Middle Eur Construct Des Cars (MECCA) 2005; 3:30-39.

[15] Rahim R, Mamat R, Taib MY, Abdullah AA. Influence of fuel temperature on diesel engine performance operating with biodiesel blend. J Mech Eng Sci. 2012; 2:

226-36.

[16] Payri R, Salvador FJ, Martí-Aldaraví P, Martínez-López J. Using one-dimensional modelling to analyse the influence of the use of biodiesels on the dynamic behaviour of solenoid-operated injectors in common rail systems: Detailed injection system model. Energy Conversion and Management 2012, 54: 90-99.

[17] Salvador FJ, Plazas AH, Gimeno J, Carreres M. Complete modelling of a piezo actuator last-generation injector for diesel injection systems. International J of Engine Research 2014; 15 (1): 3-19.

[18] Holland JH. Adaptation in natural and artificial systems. Ann Arbor: University of Michigan Press; 1975

[19] Gen M, Cheng R. Genetic algorithms and engineering design. London: Wiley; 1997.

[20] D.E. Goldberg. Genetic algorithms in search, optimization and machine learning Addison Wesley Publishing Company Inc; 1989.

[21] Abdullah K, David WC, Alice ES, 2006. Multi-objective optimization using genetic algorithms: A tutorial. Reliability Engineering and System Safety; 91: 992-1007.

[22] Deb K, Pratap A, Agarwal S, Meyarivan T. A fast and elitist multiobjective genetic algorithm: NSGA-II. Evol Comput 2002, 6 (2): 182-197.

[23] DAS I and Dennis JE. Normal-boundary intersection: a new method for generating the Pareto surface in nonlinear multicriteria optimization problems. Society for Industrial and Applied Mathematics 1988; 8(3): 631-657.

[24] Box GEP and Wilson KB. On the experimental attainment of optimum conditions

(with discussion). Journal of the Royal Statistical Society Series B 1951; 13(1): 1-45.

[25] Poles S, Lovison A. Shepard's and k-nearest's methods in the newly implemented response surfaces. modeFRONTIER help, Technical Report 2006-004; 2006.

[26] Payri R, Salvador FJ, Carreres M, De la Morena J. Fuel temperature influence on the performance of a last generation common-rail diesel ballistic injector. Part II: 1D model development, validation and analysis. Energy Conversion and Management 2016; 114: 376–391.

[27] Shi Y and Reitz RD. Assessment of optimization methodologies to study the effects of bowl geometry, spray targeting and swirl ratio for a heavy-duty diesel engine operated at high-load. SAE Int. J. Engines 2008; 1(1): 537-557.

[28] User manual of modeFRONTIER, 2014.